Proton capture reaction rates in the *rp* process

H. Herndl,* J. Görres, and M. Wiescher
Department of Physics, University of Notre Dame, Notre Dame, Indiana 46556

B. A. Brown
Department of Physics and Astronomy, and National Superconducting Cyclotron Laboratory, Michigan State University, East Lansing, Michigan 48824

L. Van Wormer
Hiram College, Hiram, Ohio 44234
(Received 10 March 1995)

Detailed shell-model calculations have been performed to study the structure of excited states in neutron deficient T=1, T=3/2, and T=2 nuclei in the mass range A = 23–43. Excitation energies, single-particle spectroscopic factors, as well as γ-transition strengths were computed. On the basis of these results new reaction rates were calculated for proton capture on the T=1/2 nucleus ^{35}Ar, on the odd-odd T=1 nuclei ^{24}Al and ^{32}Cl, on the even-even T=1 nuclei ^{26}Si, ^{30}S, ^{34}Ar, and ^{42}Ti and the T=3/2 nuclei ^{23}Al, ^{27}P, ^{31}Cl, and ^{35}K. The new reaction rates are compared with the results of statistical model calculations as well as with previous estimates. The consequences of these new rates for the reaction flow and the *rp* process nucleosynthesis at different stellar temperature and density conditions will be discussed.

PACS number(s): 25.40.Lw, 21.10.Jx, 21.60.Cs, 97.10.Cv

I. INTRODUCTION

The hot CNO cycles and the *rp* process are the dominant reaction sequences for nucleosynthesis and energy production in hot stellar hydrogen burning [1–3]. While many of the nuclear reactions in the CNO cycles have been experimentally determined [4], most of the proton capture rates on unstable nuclei in the hot CNO cycles are still uncertain [5,6]. Most of the capture rates, even on stable nuclei along the *rp* process path have not been determined experimentally. Therefore the present nucleosynthesis calculations are based on very limited, experimental information.

Proton capture reactions on isotopes ($A \geq 20$) near the line of stability typically have high Q values, $Q \geq 5$ MeV. Their reaction rates can be approximated by statistical model calculations because of the high level densities in the compound nuclei at these excitation energies [7,8].

In the case of low level densities in the compound nucleus the statistical model approach becomes invalid. Especially for neutron deficient nuclei near the proton drip line and near shell closures, proton capture reactions are characterized by small Q values and therefore the reaction rate is determined by single resonances and by nonresonant reaction contributions. Previous estimates of the reaction rates were based on the structure of the better known mirror nuclei [9,3] because no, or only very limited experimental data are available about the level structure in the particular compound nuclei.

However, many of the input parameters like resonance energies, single-particle amplitudes, proton and γ widths carry substantial uncertainties. Neither level shift energies between the mirror states nor proton partial widths could be calculated reliably, because the single-particle amplitudes of many of the resonance states were not known.

In the present work we attempt to improve the situation by calculating the level structure and the level parameters of the compound nuclei for crucial proton capture reactions along the proposed *rp* process path [3] using the results of large-basis shell-model calculations. Similar calculations for the reaction rates involving individual proton-rich nuclei have been carried out before [10–13] but this is the first systematic approach to describe all proton capture reactions in the mass $A = 23 - 43$ range where statistical Hauser-Feshbach rates might be misleading.

In the following sections we will discuss the shell-model calculations and the resulting resonant and nonresonant reaction rates. We will compare these rates with the previous estimates. We will finally implement the present rates into the reaction network to investigate their influence on the reaction flow and the evolution of the isotopic abundances in the mass range $A \leq 44$.

*Permanent address: Inst. für Kernphysik, TU Wien, A-1040 Wien, Austria.

II. SHELL-MODEL CALCULATIONS

The proton capture reactions discussed here typically have low Q values, $Q \leq 4$ MeV. The level densities in this excitation range of the compound nuclei are low and the reaction rate is dominated by one or a few resonances only. To determine a reliable reaction rate for a wide temperature range, both the resonant as well as the nonresonant reaction components have to be determined. For each resonance the contribution to the rate depends on the particular resonance energy E_r and the resonance strength $\omega\gamma$ and is expressed as a function of temperature T_9 (in 10^9 K) by [14]

$$N_A\langle\sigma v\rangle_r = 1.54 \times 10^{11}(AT_9)^{-3/2}\omega\gamma[\mathrm{MeV}]\exp\left(\frac{-11.605E_r[\mathrm{MeV}]}{T_9}\right)\mathrm{cm}^3\,\mathrm{s}^{-1}\,\mathrm{mol}^{-1}. \quad (1)$$

The reduced mass A is given by $A_pA_T/(A_p + A_T)$ where A_p is the projectile mass and A_T is the target mass. The resonance strength $\omega\gamma$ depends on the spin J_T of the target, the spin J of the resonance state, the partial width Γ_p for the entrance channel, the partial width Γ_γ for the exit channel, and the total width Γ_{tot},

$$\omega\gamma = \frac{2J+1}{2(2J_T+1)}\frac{\Gamma_p \times \Gamma_\gamma}{\Gamma_{\mathrm{tot}}}. \quad (2)$$

The proton widths are obtained by multiplying the single-particle width with the single-particle spectroscopic factor obtained from the shell-model wave functions,

$$\Gamma_p = C^2S \times \Gamma_{\mathrm{sp}}, \quad (3)$$

where the single-particle widths Γ_{sp} were calculated from the scattering phase shifts in a Woods-Saxon potential [11,12] with the potential depths determined by matching the resonance energies.

The γ widths are calculated from the electromagnetic reduced transition probabilities $B(J_i \rightarrow J_f;\mathrm{L})$ which carry the nuclear structure information of the resonance states and the final bound states [16]. The reduced transition rates were computed within the framework of the shell model. Most of the transitions in this work are $M1$ or $E2$ transitions. For these the relations are

$$\Gamma_{E2}[\mathrm{eV}] = 8.13 \times 10^{-7}E_\gamma^5[\mathrm{MeV}]B(E2)[e^2\,\mathrm{fm}^4] \quad (4)$$

and

$$\Gamma_{M1}[\mathrm{eV}] = 1.16 \times 10^{-2}E_\gamma^3[\mathrm{MeV}]B(M1)[\mu_N^2]. \quad (5)$$

The nonresonant (p,γ) reaction cross sections are mainly determined by direct capture transitions to the ground states and low excited states in the final nuclei. The nonresonant reaction rates can be calculated in terms of the astrophysical S factor $S(E_0)$ in the energy range of the Gamow window [15],

$$N_A\langle\sigma v\rangle_{\mathrm{nr}} = 7.83 \times 10^9\left(\frac{Z}{AT_9^2}\right)^{1/3}S(E_0)[\mathrm{MeV\,b}]\exp\left(-4.29\left[\frac{Z^2A}{T_9}\right]^{1/3}\right), \quad (6)$$

where Z denotes the proton number of the target nucleus. The total S factors

$$S(E_0) = \sum_i \sigma_i C^2S_iE_0\exp(2\pi\eta), \quad (7)$$

are calculated for all $E1$ transitions to bound states in the final nuclei; η denotes the Sommerfeld parameter. The single-particle cross sections σ_i have been derived in terms of a nuclear potential model [9] using a Woods-Saxon potential for the calculation of the final state wave functions. The single-particle cross sections are scaled with the spectroscopic factors C^2S_i of the final states, which are directly obtained from the shell-model calculations. The total reaction rate is the sum over all resonant and nonresonant contributions.

The excitation energies, the single-particle spectroscopic factors, and the reduced electromagnetic transition probabilities have been calculated from the shell-model wave functions of the different states. The shell-model calculations have been performed with the computer code OXBASH [17]. The code uses the m scheme but constructs basis states with good J and T with a projection technique. The Hamiltonian is formulated in this projected basis and then diagonalized with the Lanczos algorithm. Most of the reactions are in the mass region $20 \leq A \leq 40$, therefore the isotopes can be described by sd-shell configurations. The Wildenthal interaction [18] has successfully described many features of sd-shell nuclei [19]. There is one state of non-normal parity in the reaction $^{35}\mathrm{Ar}(p,\gamma)^{36}\mathrm{K}$ for which we need to include

excitations from the *sd* into the *fp* shell. The Warburton-Becker-Millener-Brown (WBMB) interaction, derived by Warburton *et al.* [21], is suitable to describe this state. For the reaction ^{42}Ti (p,γ) ^{43}V we used the interaction of Richter *et al.* [22]. It describes nuclei in the lower part of the *fp* shell, where the model space is generated by the $0f_{7/2}$, $0f_{5/2}$, $1p_{3/2}$, and $1p_{1/2}$ orbits.

The wave functions were used to calculate single-particle spectroscopic amplitudes and electromagnetic transition rates. While the calculation of spectroscopic amplitudes is straightforward, there is some freedom in the computation of the transition rates. It is well known that the transitions cannot be described satisfactorily when using free-nucleon operators. In that case the effects of configurations outside the shell-model space are not included. Effective operators are formulated to account for such effects. For the *sd* shell, effective operators for $M1$ and $E2$ transitions were determined by [23,24]. These were used in this work to calculate the transition rates.

Since most of the isotopes we consider are unstable and proton-rich, it is necessary to include the Ormand-Brown Coulomb and charge-dependent interactions which are adjusted to reproduce the isobaric mass shifts [20]. These terms are added to the Wildenthal interaction. In most cases the excitation energies of the neutron-rich mirror nuclei are known. Matrix elements of the Ormand-Brown Coulomb and charge-dependent interactions [20] were used to calculate the displacement energy between the neutron-rich and the proton-rich mirror states. We note, however, that the Ormand-Brown interaction matrix elements were obtained with harmonic-oscillator radial wave functions and the calculated shifts do not account for the large Thomas-Ehrman shift observed for loosely bound states [20]. Thus, for the nuclei with $A \leq 32$ the Thomas-Ehrman shift [25] was taken into account additionally. This downward Thomas-Ehrman shift is associated with the large rms radius of the loosely bound $1s_{1/2}$ protons and the associated smaller Coulomb interaction with the core protons.

We calculated the Thomas-Ehrman shift for a nucleus (Z,A) as follows. The Ormand-Brown matrix elements provide a good description of the displacement energy for those states which are predominantly $0d_{5/2}$ in structure. Thus we first calculate the Thomas-Ehrman effect for the difference between a pure $0d_{5/2}$ and a pure $1s_{1/2}$ single-particle state. The energy shifts are determined for a Woods-Saxon nuclear potential plus a Coulomb potential, where the nuclear potentials are the same for protons and neutrons. The shifts are given by $\epsilon_p(0d_{5/2}) - \epsilon_n(0d_{5/2})$ and $\epsilon_p(1s_{1/2}) - \epsilon_n(1s_{1/2})$, respectively, where the subscripts p and n refer to proton and neutron. The relative Thomas-Ehrman shift which depends primarily on the Q value for the proton decay Q_p and the charge Z of the proton-rich nucleus is then given by the difference

$$\delta E_{\mathrm{TE}}(Q_p,Z) = [\epsilon_p(0d_{5/2}) - \epsilon_n(0d_{5/2})] - [\epsilon_p(1s_{1/2}) - \epsilon_n(1s_{1/2})]. \quad (8)$$

The final Thomas-Ehrman shift for a particular proton-rich state with mass and charge (A,Z) is obtained by weighting the $\delta E_{\mathrm{TE}}(Q_p,Z)$ by the spectroscopic factors $S(1s_{1/2})$ for picking up a proton in the $1s$ state leading to all states of the core nucleus with mass and charge $(A-1,Z-1)$.

$$\delta E_{\mathrm{TE}} = \sum_i S_i(1\mathrm{s}_{1/2})\delta E_{\mathrm{TE}}(Q_{pi},Z), \quad (9)$$

where $\delta E_{\mathrm{TE}}(Q_p,Z)$ is given by Eq. (8). The method was tested for several states in the lower half of the *sd* shell. In almost all cases the experimental energies of the mirror nucleus could be reproduced to within 100 keV. Above $A = 32$ the $1s_{1/2}$ spectroscopic factors are small and the δE_{TE} can be neglected. Also the Thomas-Ehrman shift for the $0d_{3/2}$ state is small.

In Tables I and II the spins, energies, and spectroscopic factors of the proton bound states and the unbound resonance states are listed. The calculated energies E_x^m(calc) are the results of the Ormand-Brown interaction for the neutron-rich mirror nuclei. They are compared with the known experimental energies E_x^m(expt.). The fourth and fifth columns give the Ormand-Brown and Thomas-Ehrman shift (for $A \leq 32$) relative to the ground state. The resulting proton-rich excitation energies are listed in the sixth column. In the few cases where an experimental energy was available the calculated energy is given in brackets. The spectroscopic factors for the transitions to the bound states are needed to calculate the direct contributions to the reaction rate. For the resonance states we have highlighted in boldface the spectroscopic amplitude with the strongest contribution to the proton widths. The transfer of $j = 7/2$ is of course not possible for pure *sd*-shell configurations.

III. DISCUSSION OF THE REACTION RATES

New reaction rates were calculated for proton capture reactions with low level densities in the compound nucleus. Of particular interest are bottleneck reactions and proton captures on waiting point nuclei [3]. The following discussion includes proton captures on the $T = 1/2$ nucleus ^{35}Ar and on the odd-odd $T = 1$ nuclei ^{24}Al and ^{32}Cl. These reactions are considered bottlenecks for the reaction flow because at temperatures $T \geq 3\times10^8$ K they influence the break out from the SCl cycle (for details see

TABLE I. Excitation energies and spectroscopic amplitudes of proton bound states.

J^π	E_x^m (calc)	E_x^m (expt)	δE_c	$\delta E_{\rm TE}$	E_x	$C^2S_{1/2}$	$C^2S_{3/2}$	$C^2S_{5/2}$	$C^2S_{7/2}$
				^{23}Al $J=\frac{5}{2},T=\frac{3}{2}\rightarrow{}^{24}$Si $T=2$		$Q=3.3$ MeV			
0_1^+	0.0	0.0			0.0			3.461	
2_1^+	2.10	1.98	0.02	−0.05	1.95	0.204	0.025	0.199	
				^{24}Al $J=4,T=1\rightarrow{}^{25}$Si $T=\frac{3}{2}$		$Q=3.41$ MeV			
$\frac{5}{2}^+_1$	0.0	0.0			0.0		0.004	0.53	
$\frac{3}{2}^+_1$	0.13	0.09	0.00	−0.01	0.04(0.08)			0.784	
$\frac{3}{2}^+_2$	2.12	2.20	−0.02	−0.06	1.96(2.12)			0.007	
$\frac{9}{2}^+_1$	2.49	2.42	0.02	−0.04	2.37(2.40)	0.051	0.045	0.003	
$\frac{7}{2}^+_1$	2.73	2.79	−0.09	−0.19	2.61(2.51)	0.618	0.005	0.096	
$\frac{5}{2}^+_2$	2.79	2.91	0.01	−0.10	2.82		0.00001	0.008	
$\frac{9}{2}^+_2$	3.14		−0.08	−0.10	2.96	0.329	0.165	0.177	
$\frac{7}{2}^+_2$	2.96		0.03	−0.02	2.97	0.033	0.001	0.008	
$\frac{3}{2}^+_3$	3.29	3.35	−0.07	−0.09	3.19			0.003	
$\frac{3}{2}^+_4$	3.61	3.45	−0.04	−0.05	3.36			0.100	
				^{26}Si $J=0,T=1\rightarrow{}^{27}$P $T=\frac{3}{2}$		$Q=0.86$ MeV			
$\frac{1}{2}^+_1$	0.0	0.0			0.0	0.463			
				^{27}P $J=\frac{1}{2},T=\frac{3}{2}\rightarrow{}^{28}$S $T=2$		$Q=2.4$ MeV			
0_1^+	0.0	0.0			0.0	0.705			
2_1^+	1.51	1.47	0.02	0.04	1.53		0.301	0.057	
				^{30}S $J=0,T=1\rightarrow{}^{31}$Cl $T=\frac{3}{2}$		$Q=0.3$ MeV			
$\frac{3}{2}^+_1$	0.0	0.0			0.0		0.584		
				^{31}Cl $J=\frac{3}{2},T=\frac{3}{2}\rightarrow{}^{32}$Ar $T=2$		$Q=2.4$ MeV			
0_1^+	0.0	0.0			0.0		1.905		
2_1^+	2.07	1.94	−0.02	0.01	1.93	0.008	0.666	0.055	
				^{32}Cl $J=1,T=1\rightarrow{}^{33}$Ar $T=\frac{3}{2}$		$Q=3.34$ MeV			
$\frac{1}{2}^+_1$	0.0	0.0			0.0	0.080	0.672		
$\frac{3}{2}^+_1$	1.56	1.43	−0.04		1.34(1.39)	0.0006	0.185	0.004	
$\frac{5}{2}^+_1$	1.98	1.85	−0.03		1.79(1.82)		0.145	0.006	
$\frac{3}{2}^+_2$	2.67	2.54	−0.07		2.47	0.031	0.167	0.014	
$\frac{3}{2}^+_3$	3.61	3.27	−0.12		3.15	0.068	0.516	0.003	
				^{34}Ar $J=0,T=1\rightarrow{}^{35}$K $T=\frac{3}{2}$		$Q=0.08$ MeV			
$\frac{3}{2}^+_1$	0.0	0.0			0.0		0.364		
				^{35}Ar $J=\frac{3}{2},T=\frac{1}{2}\rightarrow{}^{36}$K $T=1$		$Q=1.67$ MeV			
2_1^+	0.0	0.0			0.0	0.008	0.755	0.002	
3_1^+	0.82	0.79	−0.02		0.80(0.77)		0.192	0.003	
1_1^+	1.24	1.16	−0.04		1.12(1.12)	0.072	0.184	0.008	
1_2^+	1.60	1.60	−0.07		1.59(1.53)	0.028	0.028	0.001	
				^{35}K $J=\frac{3}{2},T=\frac{3}{2}\rightarrow{}^{36}$Ca $T=2$		$Q=2.56$ MeV			
0_1^+	0.0	0.0			0.0		3.649		
				^{42}Ti $J=0,T=1\rightarrow{}^{43}$V $T=\frac{3}{2}$		$Q=0.09$ MeV			
$\frac{7}{2}^-_1$	0.0	0.0			0.0				0.750

TABLE II. Excitation energies and spectroscopic amplitudes of resonance states.

J^π	E_x^m (calc)	E_x^m (expt)	δE_c	$\delta E_{\rm TE}$	E_x	$C^2S_{1/2}$	$C^2S_{3/2}$	$C^2S_{5/2}$	$C^2S_{7/2}$
			^{23}Al $J=\frac{5}{2},T=\frac{3}{2}\rightarrow{}^{24}$Si $T=2$		$Q=3.3$ MeV				
2_2^+	3.69	3.87	−0.02	−0.23	3.62	**0.500**	0.000 07	0.14	
4_1^+	3.90	3.96	0.08	0.01	4.05		**0.012**	0.001	
0_2^+	4.65	4.76	−0.10	−0.49	4.17			**0.203**	
3_1^+	4.54	4.89	−0.11	−0.31	4.47	**0.491**	0.138	0.088	
			^{24}Al $J=4,T=1\rightarrow{}^{25}$Si $T=\frac{3}{2}$		$Q=3.41$ MeV				
$\frac{5}{2}^+_3$	3.63	3.69	−0.05	−0.04	3.60		0.010	**0.017**	
$\frac{9}{2}^+_3$	3.90	3.95	−0.05	−0.11	3.82 (3.79)	**0.023**	0.144	0.027	
$\frac{7}{2}^+_3$	3.97	3.93	−0.03	0.01	3.91	**0.011**	0.155	0.039	
$\frac{5}{2}^+_4$	4.04	4.14	−0.06	−0.16	3.92		0.000 05	**0.042**	
$\frac{5}{2}^+_5$	4.19	4.34	−0.04	−0.16	4.14		0.00 01	**0.001**	
			^{26}Si $J=0,T=1\rightarrow{}^{27}$P $T=\frac{3}{2}$		$Q=0.86$ MeV				
$\frac{3}{2}^+_1$	0.87	0.98	0.06	0.14	1.18		**0.414**		
$\frac{5}{2}^+_1$	1.64	1.7	0.02	0.01	1.66(1.73)			**0.126**	
			^{27}P $J=\frac{1}{2},T=\frac{3}{2}\rightarrow{}^{28}$S $T=2$		$Q=2.4$ MeV				
0_2^+	3.81	3.86	−0.1	−0.26	3.5	**0.586**			
			^{30}S $J=0,T=1\rightarrow{}^{31}$Cl $T=\frac{3}{2}$		$Q=0.3$ MeV				
$\frac{1}{2}^+_1$	0.81	0.75	0.06	0.01	0.82	**0.219**			
$\frac{5}{2}^+_1$	1.58	1.69	0.03	0.05	1.77			**0.019**	
			^{31}Cl $J=\frac{3}{2},T=\frac{3}{2}\rightarrow{}^{32}$Ar $T=2$		$Q=2.4$ MeV				
2_2^+	4.20	4.23	−0.11	−0.10	4.02	**0.062**	0.643	0.003	
			^{32}Cl $J=1,T=1\rightarrow{}^{33}$Ar $T=\frac{3}{2}$		$Q=3.34$ MeV				
$\frac{5}{2}^+_2$	3.80	3.49	−0.06		3.43		**0.021**	0.008	
$\frac{7}{2}^+_1$	3.97	3.63	−0.07		3.56			**0.003**	
$\frac{5}{2}^+_3$	3.88	4.05	−0.08		3.97		**0.041**	0.002	
$\frac{1}{2}^+_2$	4.24		−0.05		4.19	**0.067**	0.034		
$\frac{3}{2}^+_4$	5.01	4.86	−0.13		4.73	**0.003**	0.035	0.004	
			^{34}Ar $J=0,T=1\rightarrow{}^{35}$K $T=\frac{3}{2}$		$Q=0.08$ MeV				
$\frac{1}{2}^+_1$	1.57	1.57	0.00		1.57	**0.113**			
			^{35}Ar $J=\frac{3}{2},T=\frac{1}{2}\rightarrow{}^{36}$K $T=1$		$Q=1.67$ MeV				
2_2^+	2.05	1.96	−0.04		1.89(1.92)	**0.055**	0.004	0.011	
3_1^-	2.09	2.47			2.27		**0.032**	0.001	0.764
2_3^+	2.50	2.49	−0.03		2.41(2.46)	**0.038**	0.00 05	0.017	
			^{35}K $J=\frac{3}{2},T=\frac{3}{2}\rightarrow{}^{36}$Ca $T=2$		$Q=2.56$ MeV				
2_1^+	3.43	3.29	−0.03		3.26	**0.009**	0.010	0.002	
			^{42}Ti $J=0,T=1\rightarrow{}^{43}$V $T=\frac{3}{2}$		$Q=0.09$ MeV				
$\frac{5}{2}^-_1$	0.51	0.37	−0.01		0.36			**0.008**	
$\frac{3}{2}^-_1$	0.90	0.59	−0.04		0.55		**0.014**		

also [13]).

It is also important to consider the proton captures on the even-even $T = 1$ nuclei ^{26}Si, ^{30}S, ^{34}Ar, and ^{42}Ti. These reactions typically have very small Q values and are thought to be strongly hindered by inverse photodisintegration of the $T = 3/2$ compound nuclei at high temperature conditions. The photodisintegration rate, $\lambda_{(\gamma,p)_{T=3/2}}$ will exceed the proton capture rate, $\lambda_{(p,\gamma)_{T=1}}$, if $Q/kT \leq 24$ [3]. This will cause an enrichment of the $T = 1$ isotopes before they β decay. Due to their fairly long β-decay lifetimes these isotopes represent waiting points for the reaction flow. Because of the rapid equilibrization between (p,γ) and (γ,p) reactions the abundances of the $T = 1$ and $T = 3/2$ nuclei are in equilibrium and the abundance ratio is determined by the Q value as outlined by Van Wormer *et al.* [3],

$$\frac{Y_{(T=1)}}{Y_{(T=3/2)}} = \frac{\lambda_{(\gamma,p)_{T=3/2}}}{\lambda_{(p,\gamma)_{T=1}}} = 1.974 \times 10^{10} (AT_9)^{3/2} \frac{G_{T=1}}{G_{T=3/2}} \rho^{-1} \exp\left(-\frac{11.605 \times Q}{T_9}\right) \quad (10)$$

with λ as the reaction rate in units 1/s, and $G_{T=3/2}$, $G_{T=1}$ denoting the partition functions of the nuclei. The waiting point condition is reached for all T=1 nuclei at temperatures $T_9 \geq 0.14$ except for ^{26}Si. The relatively large Q value, $Q = 0.86$ MeV for ^{26}Si(p,γ)^{27}P requires a higher temperature $T_9 \geq 0.42$ for the equilibrium state between ^{26}Si and ^{27}P. For lower temperatures the abundance of ^{26}Si depends therefore strongly on the reaction rate of ^{26}Si(p,γ)^{27}P.

However, fast depletion processes—either via (p,γ) or β decay—of the $T = 3/2$ nuclei ^{23}Al, ^{27}P, ^{31}Cl, ^{35}K, and ^{43}V, will influence the equilibrium abundance of the $T = 1$ waiting point isotopes. They might be destroyed considerably faster via sequential two-proton capture, $\lambda_{(p,\gamma)_{T=1}}$, $\lambda_{(p,\gamma)_{T=3/2}}$ or/and proton capture followed by β decay, $\lambda_{(p,\gamma)_{T=1}}$, $\lambda_{\beta_{T=3/2}}$ then by the typically slow β decay. Using the notation of Van Wormer *et al.* [3] the equilibrium ratio is then given by

$$\frac{Y_{(T=1)}}{Y_{(T=3/2)}} = \frac{\lambda_{(\gamma,p)_{T=3/2}}}{\lambda_{(p,\gamma)_{T=1}}} + \frac{\lambda_{(p,\gamma)_{T=3/2}}}{\lambda_{(p,\gamma)_{T=1}}} + \frac{\lambda_{\beta_{T=3/2}}}{\lambda_{(p,\gamma)_{T=1}}}. \quad (11)$$

This is a dynamical equilibrium, with a rapid destruction of $Y_{T=3/2}$ via a subsequent fast proton capture reaction or β decay also the abundance of the preceeding $T = 1$ isotopes, $Y_{T=1}$ will drop rapidly. Most of these reactions have been considered before as important for the reaction flow and reaction rates have been estimated [1,3,9]. Because the level structure of the compound nuclei of the various reactions is not very well known the previous estimates are typically based on the experimentally much better known states in the respective mirror nuclei. No level shift considerations were taken into account in estimating the resonance energies. Also the single-particle spectroscopic factors and γ-partial widths for the different resonance levels were estimated, because in most of the cases discussed here, no structure information was available for the mirror states. This introduces considerable uncertainties into the rates, which will be reduced with the theoretically improved treatment of the level structure presented here. In the following discussion of the single reaction rates the present results are compared with the previous estimates [9,3].

A. ^{35}Ar(p,γ) ^{36}K (Q=1.67 MeV)

Three resonance states are included, all have been observed in transfer reaction studies [26]. The experimental uncertainty in the excitation energies is $\pm$30 keV. The 3^-_1 level is characterized by a 1p1h excitation into the $0f_{7/2}$ shell. This is supported by the high spectroscopic factors for a $j = 7/2$ transfer to this state. We used the experimental energy of 2.27 MeV [26] for calculating its contribution to the reaction rate. The 2^+_2 state has an

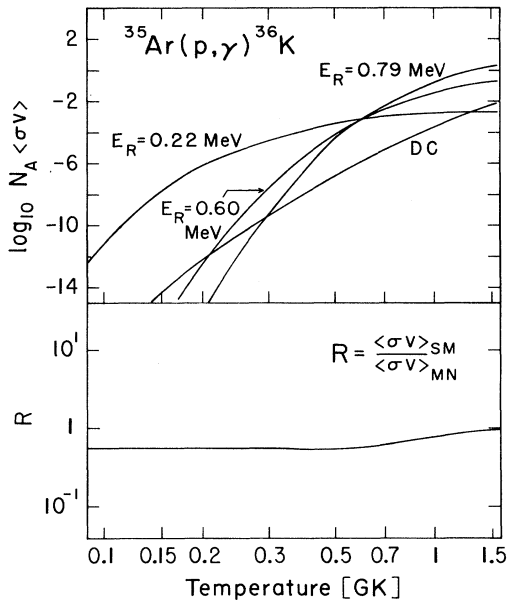

FIG. 1. The reaction rate of ^{35}Ar$(p,\gamma)^{36}$K is dominated by the contributions of the resonance at 220 keV and 790 keV as seen in the upper part of the figure. The contributions of the resonance at 600 keV and the direct capture (DC) are negligible. The lower part shows the ratio between the present reaction rate $\langle\sigma v\rangle_{\rm SM}$, based on the shell-model predictions for the level parameters, and the previous estimate $\langle\sigma v\rangle_{\rm MN}$, based on the experimentally known parameters of the mirror states in ^{36}Cl. The ratio indicates good agreement between the two predictions.

TABLE III. Nonresonant direct capture transitions and the astrophysical S factors; resonance energies, γ widths, proton widths, and resonance strengths for $^{35}\mathrm{Ar}(p,\gamma)^{36}\mathrm{K}$.

			$^{35}\mathrm{Ar}(p,\gamma)^{36}\mathrm{K}$ $Q = 1.67$ MeV		
E_x	J^π	ℓ_i	$n\ell_f$	C^2S_f	$S(E_0)$ (MeV b)
0.00	2_1^+	p	$2s_{1/2}$	0.008	2.34×10^{-3}
		p	$1d_{3/2}$	0.755	1.60×10^{-2}
0.80	3_1^+	p	$1d_{3/2}$	0.192	4.35×10^{-3}
1.12	1_1^+	p	$2s_{1/2}$	0.072	1.50×10^{-2}
		p	$1d_{3/2}$	0.184	1.35×10^{-3}
1.59	1_2^+	p	$2s_{1/2}$	0.028	4.68×10^{-3}
		p	$1d_{3/2}$	0.028	1.16×10^{-4}
E_x	E_p	J^π	Γ_γ (eV)	Γ_p (eV)	$\omega\gamma$ (eV)
1.89	0.22	2_2^+	6.76×10^{-3}	2.49×10^{-7}	1.56×10^{-7}
2.27	0.60	3_1^-	2.64×10^{-4}	1.21×10^{-1}	2.31×10^{-4}
2.41	0.74	2_3^+	1.34×10^{-2}	6.79	8.39×10^{-3}

experimental energy of 1.89 MeV while the theoretically predicted energy is 1.92 MeV. For the 2_3^+ we took the experimentally known energy of 2.41 MeV which is in good agreement with the calculated excitation energy of 2.46 MeV. The spin assignment for the observed levels is, however, based on the previous mirror assignment [3] for these two states. The partial widths and the resonance strengths of the levels are listed in Table III. The direct capture to the ground state and the first two excited states was calculated as described above. The contributions of the various transitions are also listed in Table III. The present reaction rate is shown in Fig. 1 as a function of temperature. It indicates that all three resonances contribute significantly, while the direct capture is negligible. The rate is based on the same experimental energies as in the previous estimate, the resonance strengths are only slightly different because of the generally good agreement between the computed proton and γ partial widths and the corresponding partial widths of the mirror states. The shell-model based reaction rate is therefore in good agreement with the previous estimate. No change for the predicted reaction flow and nucleosynthesis in this mass range [3] is anticipated.

B. $^{24}\mathrm{Al}(p,\gamma)$ $^{25}\mathrm{Si}(Q=3.407$ MeV)

Considered is the excitation range between 3.4 and 4.4 MeV in the compound nucleus ^{25}Si. Only one state has been observed at $E_x=3820\pm20$ keV in ^{25}Si. In the mirror nucleus ^{25}Na eight levels are known in this region, but only two of them have a clear J^π assignment [26]. The state at 3.455 MeV is most likely a $3/2^+$. Because of the large Thomas-Ehrman shift its mirror state in ^{25}Si is proton bound and therefore not considered here. The $1/2^-$ at 4.0 MeV and the $1/2^+$ at 4.29 MeV do not contribute strongly since the ground state of ^{24}Al is 4^+ and the transfer of $j = 7/2$ is negligible. These levels are therefore not included in the reaction rate. The spins of the remaining five resonance levels are uncertain; for the present calculation the spin assignment is based on the comparison with the calculated excitation energies and lifetimes. Comparison with the previous estimate [3] shows that the excitation energies and the resulting resonance energies differ considerably due to the Thomas-Ehrman shift. Also changed are the proton partial widths which have been previously estimated from an assumed single-particle spectroscopic factor of $C^2S=0.1$. This influences strongly the resulting resonance strengths which

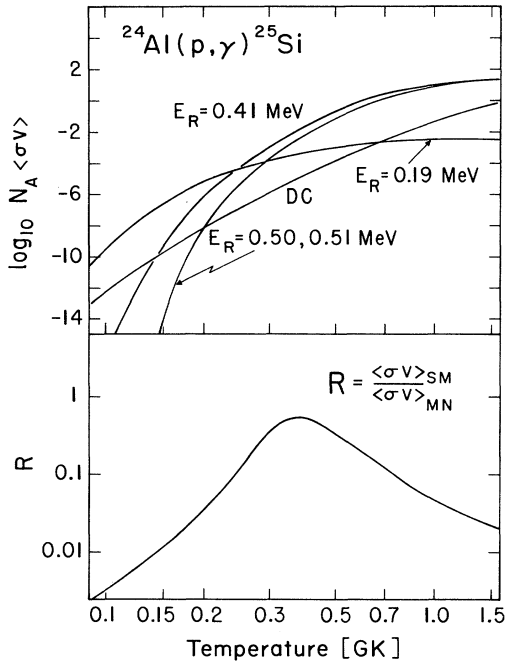

FIG. 2. The reaction rate of $^{24}\mathrm{Al}(p,\gamma)^{25}\mathrm{Si}$ is dominated by the contributions of the resonance at 190 keV and 380 keV as seen in the upper part of the figure. The resonances at 500 and 510 keV contribute at temperatures above 1.5×10^9 K. The direct capture (DC) contributions are negligible. Also presented is the ratio between the present reaction rate $\langle\sigma v\rangle_{\mathrm{SM}}$, based on the shell-model predictions for the level parameters, and the previous estimate $\langle\sigma v\rangle_{\mathrm{MN}}$, based on the experimentally known parameters of the mirror states in ^{25}Na. The revised rate is generally up to 2 orders of magnitude lower than the previous rate, except for the temperature range around $T=4\times10^8$K as shown in the lower part of the figure.

TABLE IV. Nonresonant direct capture transitions and the astrophysical S factors; resonance energies, γ widths, proton widths, and resonance strengths for $^{24}Al(p,\gamma)^{25}Si$.

$^{24}Al(p,\gamma)^{25}Si$ $Q = 3.41$ MeV					
E_x	J^π	ℓ_i	$n\ell_f$	C^2S_f	$S(E_0)$ (MeV b)
0.00	$\frac{5}{2}^+_1$	p	$1d_{5/2}$	0.530	7.30×10^{-4}
0.04	$\frac{3}{2}^+_1$	p	$1d_{5/2}$	0.784	7.05×10^{-4}
1.96	$\frac{3}{2}^+_2$	p	$1d_{5/2}$	0.007	3.80×10^{-6}
2.37	$\frac{9}{2}^+_1$	p	$2s_{1/2}$	0.051	1.35×10^{-3}
		p	$1d_{3/2}$	0.045	5.20×10^{-5}
2.61	$\frac{7}{2}^+_1$	p	$2s_{1/2}$	0.618	1.38×10^{-2}
		p	$1d_{5/2}$	0.096	7.80×10^{-5}
2.82	$\frac{5}{2}^+_2$	p	$1d_{5/2}$	0.008	4.70×10^{-6}
2.96	$\frac{9}{2}^+_2$	p	$2s_{1/2}$	0.329	1.01×10^{-2}
		p	$1d_{3/2}$	0.165	1.18×10^{-5}
		p	$1d_{5/2}$	0.171	1.22×10^{-5}
2.97	$\frac{7}{2}^+_2$	p	$2s_{1/2}$	0.033	7.80×10^{-4}
3.36	$\frac{3}{2}^+_4$	p	$1d_{5/2}$	0.100	2.27×10^{-5}
E_x	E_p	J^π	Γ_γ (eV)	Γ_p (eV)	$\omega\gamma$ (eV)
3.60	0.19	$\frac{5}{2}^+_3$	3.99×10^{-2}	5.66×10^{-7}	1.89×10^{-7}
3.82	0.41	$\frac{9}{2}^+_3$	1.31×10^{-2}	7.47×10^{-1}	7.2×10^{-3}
3.91	0.50	$\frac{7}{2}^+_3$	1.51×10^{-2}	2.38	6.7×10^{-3}
3.92	0.51	$\frac{5}{2}^+_4$	7.27×10^{-2}	0.1	1.4×10^{-2}
4.14	0.73	$\frac{5}{2}^+_5$	1.22×10^{-1}	5.3×10^{-2}	1.23×10^{-2}

are listed in Table IV. The S factors for possible direct capture transitions to the ground state and several excited states in ^{25}Si (listed in Table I) have been calculated and are tabulated in Table IV.

The reaction rate is presented in Fig. 2. The figure shows that in the lower temperature range $T \leq 8\times10^8$ K the reaction rate is dominated by the $J^\pi=5/2^+_3$ resonance at 190 keV and by the $9/2^+_3$ resonance at 380 keV. At higher temperatures the rate is dominated by the resonance contribution of the doublet at 500 keV ($7/2^+_3$) and 510 keV ($5/2^+_5$). At temperatures $T \leq 2\times10^8$ K the present reaction rate is considerably lower than the previous estimate. The direct capture contribution is negligible over the entire temperature range.

C. $^{32}Cl(p,\gamma)$ ^{33}Ar (Q=3.34 MeV)

No experimental information is presently available about the level structure of ^{33}Ar above the proton threshold at 3.34 MeV. The information about the mirror nucleus ^{33}P does however indicate several resonances. No strong shifts between the mirror levels are anticipated as we are approaching the upper end of the *sd* shell. The Thomas-Ehrman shift is negligible since the nucleons are tightly bound in this region. While the experiment gives two $5/2^+$ states at 4.05 and 4.19 MeV for the mirror nucleus ^{33}P, the calculation predicts one $5/2^+$ and one $1/2^+$ in this energy region. We used the theoretical energy and spin for the second state. The resonance energies and resonance strengths are given in Table V. The S factors for the direct capture transitions to the ground state and the first four excited states in ^{33}Ar are listed in Table V. The resonance and direct capture contributions to the reaction rate are shown in Fig. 3. The low energy and small resonance width of the $7/2^+_2$ state cause a lower rate compared to the previous estimate [3] at low temperatures. On the other hand, the higher resonance widths of the $5/2^+_3$ and $1/2^+_2$ increase the rate at higher temperatures by more than 1 order of magnitude compared to the previous estimate.

D. $^{23}Al(p,\gamma)$ ^{24}Si (Q=3.301 MeV)

This reaction is subsequent to $^{22}Mg(p,\gamma)^{23}Al$ which has been discussed elsewhere [10]. We have included four resonances in this reaction. Three of the ^{24}Si states, the 2^+_2, the 0^+_2, and the 3^+_1, experience a strong Thomas-Ehrman shift where the total shift for the 0^+_2 is the

TABLE V. Nonresonant direct capture transitions and the astrophysical S factors; resonance energies, γ widths, proton widths, and resonance strengths for $^{32}\mathrm{Cl}(p,\gamma)^{33}\mathrm{Ar}$.

			$^{32}\mathrm{Cl}(p,\gamma)^{33}\mathrm{Ar}$ $Q = 3.34$ MeV		
E_x	J^π	ℓ_i	$n\ell_f$	C^2S_f	$S(E_0)$ (MeV b)
0.00	$\frac{1}{2}^+_1$	p	$2s_{1/2}$	0.080	7.00×10^{-3}
		p	$1d_{3/2}$	0.672	6.14×10^{-3}
1.34	$\frac{3}{2}^+_1$	p	$1d_{3/2}$	0.185	2.62×10^{-3}
1.79	$\frac{5}{2}^+_1$	p	$1d_{3/2}$	0.145	2.74×10^{-3}
2.47	$\frac{3}{2}^+_2$	p	$2s_{1/2}$	0.031	6.16×10^{-3}
		p	$1d_{3/2}$	0.167	1.67×10^{-3}
3.15	$\frac{3}{2}^+_3$	p	$2s_{1/2}$	0.068	1.46×10^{-2}
		p	$1d_{3/2}$	0.516	3.01×10^{-3}
E_x	E_p	J^π	Γ_γ (eV)	Γ_p (eV)	$\omega\gamma$ (eV)
3.43	0.09	$\frac{5}{2}^+_2$	1.77×10^{-2}	8.7×10^{-18}	8.7×10^{-18}
3.56	0.22	$\frac{7}{2}^+_2$	1.94×10^{-3}	1.13×10^{-9}	1.51×10^{-9}
3.97	0.63	$\frac{5}{2}^+_3$	1.54×10^{-2}	2.22×10^{-2}	9.09×10^{-3}
4.19	0.85	$\frac{1}{2}^+_2$	1.54×10^{-1}	46.74	5.12×10^{-2}
4.73	1.39	$\frac{3}{2}^+_4$	8.48×10^{-2}	100.3	5.65×10^{-2}

strongest with 600 keV. The resonance energies and resonance strengths are listed in Table VI. Direct capture transitions to the ground state and the first excited state have been calculated and the S factors are listed in Table VI as well. The 2^+_2 low energy resonance at 0.32 MeV dominates the reaction rate, whereas the contributions of the other resonance states and the direct capture are negligible. The present rate is considerably larger than the previous estimates at lower temperatures as shown in Fig. 4. This, however, has only little influence on the reaction flow and the nucleosynthesis because ^{23}Al is only produced at temperatures $T \geq 2\times10^8$ K [10].

E. ^{26}Si(p,γ) ^{27}P (Q=0.86 MeV)

The ground state of ^{27}P is $1/2^+$. The strong $1s_{1/2}$ single-particle component in the wave function causes a Thomas-Ehrman shift of the ground state whereas the excited states only have small shifts. This explains the high excitation energy of the $3/2^+_1$ (compared to the energy in the mirror nucleus ^{27}Mg). This level had been neglected as subthreshold state in previous estimates [9], due to its large shift relative to the ground state, however, it has a strong influence on the reaction rate. The $5/2^+_1$ is experimentally known at 1.66 MeV in ^{27}P while the energy calculated here is 1.73 MeV. This resonance has no influence on the reaction rate. The resonance parameters are listed in Table VII. The direct capture to the ground state in ^{27}P is calculated and listed in Table VII. The resonant and direct capture contributions are shown in Fig. 5, also shown is the comparison with the previous rate [9]. The ratio indicates a considerable increase of up to 3 orders of magnitude in the temperature range of hot hydrogen burning. This has significant consequences for the nucleosynthesis in this mass range.

TABLE VI. Nonresonant direct capture transitions and the astrophysical S factors; resonance energies, γ widths, proton widths, and resonance strengths for $^{23}\mathrm{Al}(p,\gamma)^{24}\mathrm{Si}$.

			$^{23}\mathrm{Al}(p,\gamma)^{24}\mathrm{Si}$ $Q = 3.30$ MeV		
E_x	J^π	ℓ_i	$n\ell_f$	C^2S_f	$S(E_0)$ (MeV b)
0.00	0^+_1	p	$1d_{5/2}$	3.461	1.00×10^{-3}
1.95	2^+_1	p	$2s_{1/2}$	0.204	3.37×10^{-3}
		p	$1d_{3/2}$	0.025	2.22×10^{-5}
		p	$1d_{5/2}$	0.199	1.77×10^{-4}
E_x	E_p	J^π	Γ_γ (eV)	Γ_p (eV)	$\omega\gamma$ (eV)
3.62	0.32	2^+_2	1.7×10^{-2}	1.26	7.08×10^{-3}
4.05	0.75	4^+_1	7.2×10^{-4}	0.62	5.4×10^{-4}
4.17	0.87	0^+_2	3.4×10^{-4}	35.93	2.8×10^{-5}
4.47	1.17	3^+_1	7.97×10^{-3}	2.58×10^4	4.65×10^{-3}

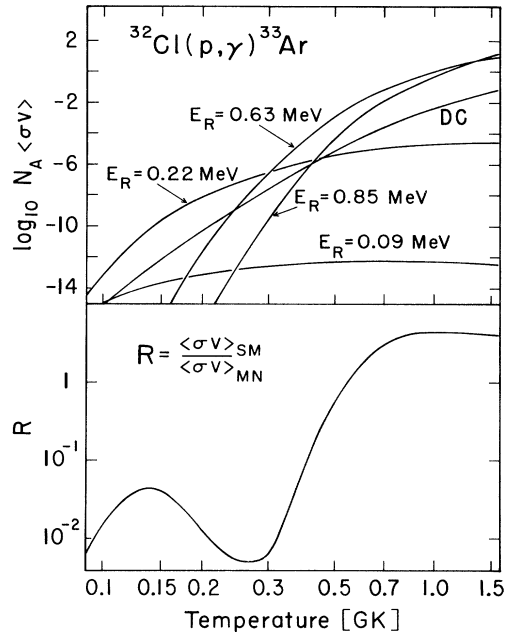

FIG. 3. The reaction rate of ^{32}Cl$(p,\gamma)^{33}$Ar is dominated by the contributions of the resonance at 220 keV and 630 keV as seen in the upper part of the figure. The contributions of the high energy resonance at 850 keV and of the direct capture transitions are negligible. The lower part shows the ratio between the present reaction rate $\langle\sigma v\rangle_{SM}$, based on the shell-model predictions for the level parameters, and the previous estimate $\langle\sigma v\rangle_{MN}$, based on the experimentally known level energies in the mirror states in ^{33}P and the assumption of a typical single-particle spectroscopic factor $C^2S = 0.05$. The comparison shows that at lower energies the present rate is considerably lower than the previous estimate, but significantly higher at temperatures above 6×10^8 K.

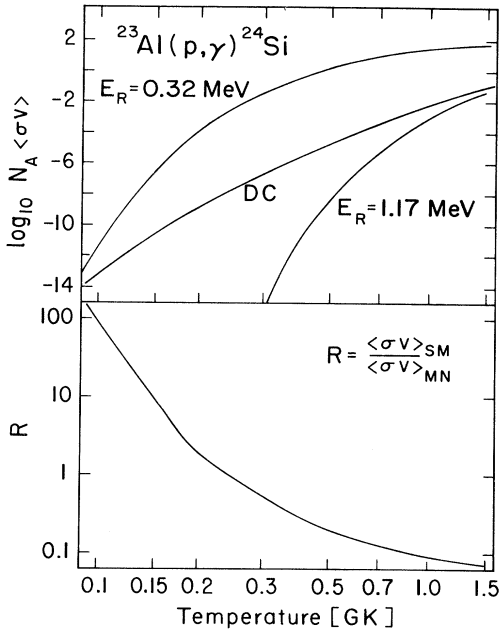

FIG. 4. The reaction rate of ^{23}Al$(p,\gamma)^{24}$Si is dominated by a single resonance at 320 keV as seen in the upper part of the figure. The direct capture contributions are several orders of magnitude smaller in the entire temperature range. The ratio between the present reaction rate $\langle\sigma v\rangle_{SM}$, based on the shell-model predictions, and the previous estimate $\langle\sigma v\rangle_{MN}$, is shown in the lower part of the figure. The deviation at lower temperatures is mainly explained by the shift of the resonance energy, an additional increase of the resonance strength yields from the large single-particle spectroscopic factors which result from the shell-model calculations.

As this present rate depends sensitively on the excitation energy of the $3/2^+_1$ state an experimental verification is highly desirable.

F. ^{27}P(p,γ) ^{28}S (Q=2.400 MeV)

As shown in Table II the 0^+_2 state is strongly shifted, but its excitation energy is still high. The resonance energy and resonance strength are listed in Table VIII. The resonance contribution to the reaction rate is negligible. Because there is no other resonance in the low energy range up to 1 MeV proton energy the direct reaction mechanism is dominating. This is in agreement with previous conclusion about the reaction mechanism [3], the present direct capture cross section (see Table VIII), however, is considerably higher than suggested before, mainly because of the large spectroscopic factors for the ground state and the first excited state in ^{28}S obtained in the present calculation (see Table I). Figure 5 shows the contributions to the reaction rate as well as the comparison with the previous estimate.

TABLE VII. Nonresonant direct capture transitions and the astrophysical S factors; resonance energies, γ widths, proton widths, and resonance strengths for ^{26}Si$(p,\gamma)^{27}$P.

			^{26}Si$(p,\gamma)^{27}$P Q = 0.86 MeV		
E_x	J^π	ℓ_i	$n\ell_f$	C^2S_f	$S(E_0)$ (MeV b)
0.00	$\frac{1}{2}^+_1$	p	$2s_{1/2}$	0.463	3.63×10^{-2}
E_x	E_p	J^π	Γ_γ (eV)	Γ_p (eV)	$\omega\gamma$ (eV)
1.18	0.32	$\frac{3}{2}^+$	1.36×10^{-3}	1.7×10^{-3}	1.51×10^{-3}
1.66	0.80	$\frac{5}{2}^+$	3.3×10^{-4}	13.61	9.9×10^{-4}

TABLE VIII. Nonresonant direct capture transitions and the astrophysical S factors; resonance energies, γ widths, proton widths, and resonance strengths for $^{27}P(p,\gamma)^{28}S$.

			$^{27}P(p,\gamma)^{28}S$ $Q = 3.30$ MeV		
E_x	J^π	ℓ_i	$n\ell_f$	C^2S_f	$S(E_0)$ (MeV b)
0.00	0_1^+	p	$2s_{1/2}$	0.705	1.74×10^{-2}
1.53	2_1^+	p	$1d_{3/2}$	0.301	1.89×10^{-3}
		p	$1d_{5/2}$	0.057	3.59×10^{-4}
E_x	E_p	J^π	Γ_γ (eV)	Γ_p (eV)	$\omega\gamma$ (eV)
3.50	1.10	0_2^+	3.4×10^{-4}	8.85×10^{3}	8.5×10^{-5}

G. $^{30}S(p,\gamma)$ ^{31}Cl (Q=0.296 MeV)

The Q value of the reaction is very low. Only the first excited state in ^{31}Cl contributes strongly as resonance at 0.52 MeV. The level parameters and the resonance strengths of both unbound states considered here are listed in Table IX. Since the first excited state is predicted to be 70 keV higher in excitation energy than the mirror state (which was previously used to calculate the resonance energy) the present rate is smaller in the temperature range $T = 10^8 - 10^9$ K. At lower temperatures the reaction rate is determined by the direct capture to the ground state (see Table IX), as shown in Fig. 6.

H. $^{31}Cl(p,\gamma)$ ^{32}Ar (Q=2.400 MeV)

Also in this case, no resonance is anticipated near the threshold. This is supported by the level structure observed in the mirror nucleus ^{32}Si. The parameters of the high energy resonance at 1.62 MeV are listed in Table X. The reaction rate is dominated by the direct capture

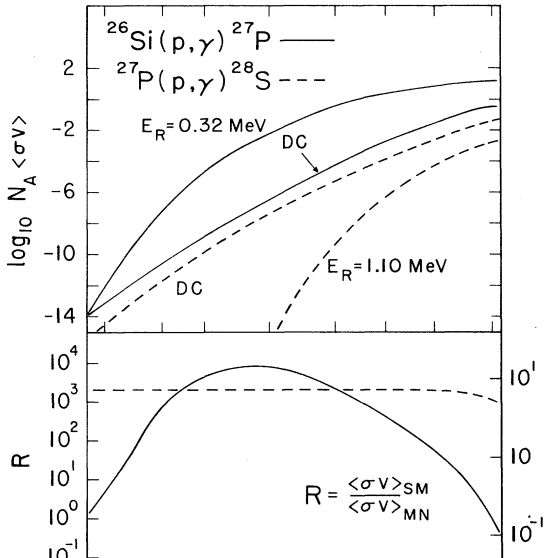

FIG. 5. The figure shows the reaction rate contributions for $^{26}Si(p,\gamma)^{27}P$ (solid lines) and for the subsequent reaction $^{27}P(p,\gamma)^{28}S$ (dashed lines). The $^{26}Si(p,\gamma)$ reaction is dominated by a strong resonance at 320 keV, which was not included in previous estimates. This explains the large enhancement of the rate by nearly 4 orders of magnitude in the temperature range 3×10^8 K as shown in the lower part of the figure. The reaction rate of $^{27}P(p,\gamma)$ is dominated by the direct capture to the ground state in ^{28}S. Because of its large single-particle spectroscopic factor the reaction rate is increased by nearly 1 order of magnitude compared to previous estimates (see right-hand scale).

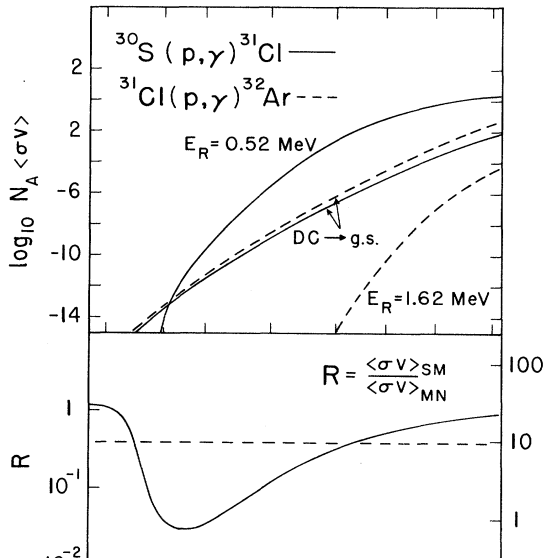

FIG. 6. The figure shows the reaction rate contributions for $^{30}S(p,\gamma)^{31}Cl$ (solid lines) and for the subsequent reaction $^{31}Cl(p,\gamma)^{32}Ar$ (dashed lines). The $^{30}S(p,\gamma)$ reaction is dominated by a strong resonance at 520 keV. The resonance energy is increased by 70 keV compared to previous estimates. This explains the deviation of the present rate in the temperature range of 2×10^8 K as shown in the lower part of the figure. The reaction rate of $^{31}Cl(p,\gamma)$ is dominated by the direct capture to the ground state in ^{32}Ar. Because of its large single-particle spectroscopic factor the reaction rate is increased by nearly 1 order of magnitude compared to previous estimates (see right-hand scale).

TABLE IX. Nonresonant direct capture transitions and the astrophysical S factors; resonance energies, γ widths, proton widths, and resonance strengths for $^{30}S(p,\gamma)^{31}Cl$.

$^{30}S(p,\gamma)^{31}Cl$ $Q = 0.30$ MeV					
E_x	J^π	ℓ_i	$n\ell_f$	C^2S_f	$S(E_0)$ (MeV b)
0.00	$\frac{3}{2}^+_1$	p	$1d_{3/2}$	0.584	5.14×10^{-3}
E_x	E_p	J^π	Γ_γ (eV)	Γ_p (eV)	$\omega\gamma$ (eV)
0.82	0.52	$\frac{1}{2}^+_1$	1.23×10^{-3}	2.95	1.23×10^{-3}
1.77	1.47	$\frac{5}{2}^+_1$	1.0×10^{-3}	35.3	3.0×10^{-3}

to the ground state and the first excited state (see Table I). The direct capture parameters are listed in Table X. The present reaction rate is 1 order of magnitude higher than previously assumed based on the large calculated ground state spectroscopic factor C^2S=1.9. The reaction rate and the comparison with the previous prediction are shown in Fig. 6.

I. ^{34}Ar(p,γ) ^{35}K (Q=0.078 MeV)

The Q value for this reaction is only 78 keV and the lowest resonance is at 1.49 MeV proton energy. No Coulomb shift is anticipated for the observed state at 1.57 MeV in the mirror nucleus ^{35}S. The resonance parameters are tabulated in Table XI. The reaction rate is entirely dominated by the direct capture to the ground state. The spectroscopic factor resulting from the shell-model calculations, C^2S=0.36, is in reasonably good agreement with the spectroscopic factor of the mirror state in ^{35}S, C^2S=0.46, which was used before. The resulting S factor for the direct capture transition is listed in Table XI. The reaction rate contributions are shown in Fig. 7.

J. ^{35}K(p,γ) ^{36}Ca (Q=2.56 MeV)

The shell-model calculations predict essentially only one resonance, which corresponds to the 2^+_1 state in ^{36}S. This is in agreement with the observed level structure in the mirror nucleus ^{36}S. The new resonance strength, listed in Table XII, is 1 order of magnitude smaller than the previously assumed one, mainly because the shell-model based γ width of the state is considerably smaller than the previously used experimental width of the mirror state in ^{36}S. The reason for this asymmetry is that the transition in ^{36}S is a pure proton excitation with a large proton effective charge of 1.35 whereas the transition in ^{36}Ca is a pure neutron excitation with a smaller neutron effective charge of 0.35. Not included in the present rate is the 0^+ state at a resonance energy of 0.79 MeV. This state is predominantly a 2p2h excitation into the fp shell. Therefore it is very difficult to calculate since the dimension in a full sd and fp shell-model space is very high. However, the spectroscopic factor and the transition to this state should be relatively small for this configuration and it was therefore neglected. Because of the large spectroscopic factor of the ground state in ^{36}Cl the direct capture component is considerably stronger than estimated before (see Table XII). The direct capture dominates the reaction rate at lower temperatures, the comparison with the previous estimate shown in Fig. 7 therefore indicates an increase of the rate in low temperature regimes and a decrease for higher temperature conditions.

K. ^{42}Ti(p,γ) ^{43}V (Q=0.09 MeV)

There are two low-lying states in ^{43}V, the $5/2^-_1$ and the $3/2^-_1$, which correspond to the first two excited states in the mirror nucleus ^{43}Ca [26] (see Table II). The Coulomb shifts are very small. They were calculated by using a charge-dependent interaction for the fp shell [20]. The resonance strength, listed in Table XIII, is clearly smaller for the $5/2^-_1$ resonance at 270 keV than previously thought [3]. This is mainly due to the small

TABLE X. Nonresonant direct capture transitions and the astrophysical S factors; resonance energies, γ widths, proton widths, and resonance strengths for $^{31}Cl(p,\gamma)^{32}Ar$.

$^{31}Cl(p,\gamma)^{32}Ar$ $Q = 2.40$ MeV					
E_x	J^π	ℓ_i	$n\ell_f$	C^2S_f	$S(E_0)$ (MeV b)
0.00	0^+_1	p	$1d_{3/2}$	1.905	4.92×10^{-2}
1.93	2^+_1	p	$1d_{3/2}$	0.666	4.45×10^{-3}
		p	$1d_{5/2}$	0.055	3.69×10^{-4}
E_x	E_p	J^π	Γ_γ (eV)	Γ_p (eV)	$\omega\gamma$ (eV)
4.02	1.62	2^+_2	1.07×10^{-4}	4.92×10^{3}	6.69×10^{-5}

TABLE XI. Nonresonant direct capture transitions and the astrophysical S factors; resonance energies, γ widths, proton widths, and resonance strengths for $^{34}\mathrm{Ar}(p,\gamma)^{35}\mathrm{Cl}$.

			$^{34}\mathrm{Ar}(p,\gamma)^{35}\mathrm{K}$	$Q = 0.08$ MeV	
E_x	J^π	ℓ_i	$n\ell_f$	C^2S_f	$S(E_0)$ (MeV b)
0.00	$\frac{3}{2_1}^+$	p	$1d_{3/2}$	0.364	1.12×10^{-2}
E_x	E_p	J^π	Γ_γ (eV)	Γ_p (eV)	$\omega\gamma$ (eV)
1.57	1.49	$\frac{1}{2_1}^+$	2.06×10^{-4}	2.8×10^{3}	2.06×10^{-4}

spectroscopic factor. For the $3/2_1^-$ resonance at 550 keV the strength is close to the previous estimate. The $3/2^+$ and $5/2^+$ states at 0.9 and 1.3 MeV proton energy are neglected because their contribution to the rate is not important if $T \leq 1.5 \times 10^9$. The direct capture to the ground state in ^{43}V has been calculated and is listed in Table XIII. Its contribution to the reaction rate is negligible over the entire temperature range. The total reaction rate and its comparison to the previous estimate is shown in Fig. 8.

The subsequent proton capture reaction $^{43}\mathrm{V}(p,\gamma)^{44}\mathrm{Cr}$ is determined by many resonances. The high level density in the mirror nucleus ^{44}Ca [26] suggests also a high level density in ^{44}Cr above the proton threshold at S_p=2.59 MeV. For this reaction we therefore adopted the Hauser-Feshbach rate calculated with SMOKER [8].

IV. REACTION FLOW AND NUCLEOSYNTHESIS

Network calculations have been performed to investigate the consequences of the modifications in the rates discussed above for the reaction flow and the nucleosynthesis in the mass range $A \leq 45$. Therefore, the calculations have been performed for constant temperature and density conditions. We calculated the reaction flow and the time-dependent abundances for all neutron deficient unstable and all stable isotopes in the mass range $20 \leq A \leq 45$ for temperatures T_9=0.15, 0.2, 0.25, 0.3, 0.4 at a constant density of $\rho = 10^4$ g/cm^3. Higher temperatures were not considered because previous calculations have shown that a more or less continous reaction flow characterizes the rp process in the lower mass regions with the β decay of the waiting points as main impedance effect [3]. For these calculations the reaction network presented in [3] has been used with the reaction rates discussed above. The results are compared with the results obtained in the previous calculations [3].

The reaction flow and abundances computed for T_9=0.15 show no changes to the results of previous computations. This is not surprising because at these low temperature conditions the reaction path is relatively close to the line of stability and the proton capture rates discussed here are in any case slower than the β decay.

For T_9=0.2 a slight enhancement in the equilibrium abundance of ^{24}Al can be observed accompanied with a reduction in ^{25}Si. This is due to the decrease of the reaction rate for $^{24}\mathrm{Al}(p,\gamma)^{25}\mathrm{Si}$ in that temperature range. This effect is however of secondary importance because the main bulk of the produced mass A=25 nuclei result from ^{25}Al. Also observed is a considerable increase of the equilibrium abundance of ^{27}P because of the much stronger $^{26}\mathrm{Si}(p,\gamma)^{27}\mathrm{P}$ rate. This increase in the proton capture rate, however, does not result in a change of the ^{26}Si abundance because this isotope is mainly depleted by β decay with a considerably larger rate than by the proton capture. The modified reaction rates had no noticable effect on the higher mass isotopic abundances.

At T_9=0.25 the considerably larger $^{26}\mathrm{Si}(p,\gamma)^{27}\mathrm{P}$ rate causes a change in the reaction flow and in the isotopic abundances in the mass $A = 26 - 28$ range. Figure 9 shows the reaction path in this mass range. The strong reaction flow via $^{26}\mathrm{Si}(p,\gamma)^{27}\mathrm{P}(\beta^+\nu)^{27}\mathrm{Si}$ causes a faster depletion of the "waiting point" isotope ^{26}Si as indicated by the previous calculations which were based on the previously estimated $^{26}\mathrm{Si}(p,\gamma)^{27}\mathrm{P}$ rate [9]. This is reflected in the time-dependent isotopic abundances shown in Fig. 10. Using the previous reaction rate, ^{26}Si is strongly enhanced after $t = 0.1$ s and remains highly enriched for a time period of 100 s. This also causes an enrichment of the β-decay daughter nucleus ^{26}Al. The use of the new rate in the network calculations, however, leads to a rapid depletion of ^{26}Si and with it ^{26}Al by nearly 2 orders of magnitude, while the abundance of ^{27}Si becomes enriched for the time period $t = 0.1 - 10.0$ s. In the higher mass regions no substantial change was caused by the introduction of the new reaction rates.

At the temperature of T_9=0.3 the change of the $^{26}\mathrm{Si}(p,\gamma)^{27}\mathrm{P}$ rate again causes a strong

TABLE XII. Nonresonant direct capture transitions and the astrophysical S factors; resonance energies, γ widths, proton widths, and resonance strengths for $^{35}\mathrm{K}(p,\gamma)^{36}\mathrm{Ca}$.

			$^{35}\mathrm{K}(p,\gamma)^{36}\mathrm{Ca}$	$Q = 2.56$ MeV	
E_x	J^π	ℓ_i	$n\ell_f$	C^2S_f	$S(E_0)$ (MeV b)
0.00	0_1^+	p	$1d_{3/2}$	3.649	2.72×10^{-2}
E_x	E_p	J^π	Γ_γ (eV)	Γ_p (eV)	$\omega\gamma$ (eV)
3.26	0.70	2_1^+	5.67×10^{-4}	2.02×10^{-1}	3.53×10^{-4}

TABLE XIII. Nonresonant direct capture transitions and the astrophysical S factors; resonance energies, γ widths, proton widths, and resonance strengths for $^{42}\mathrm{Ti}(p,\gamma)^{43}\mathrm{V}$.

			$^{42}\mathrm{Ti}(p,\gamma)^{43}\mathrm{V}$	$Q = 0.08$ MeV	
E_x	J^π	ℓ_i	$n\ell_f$	C^2S_f	$S(E_0)$ (MeV b)
0.00	$\frac{7}{2}^-_1$	d	$1f_{7/2}$	0.750	4.91×10^{-20}
E_x	E_p	J^π	Γ_γ (eV)	Γ_p (eV)	$\omega\gamma$ (eV)
0.36	0.27	$\frac{5}{2}^-_1$	1.41×10^{-5}	1.1×10^{-12}	3.3×10^{-12}
0.55	0.46	$\frac{3}{2}^-_1$	3.35×10^{-6}	2.8×10^{-5}	5.98×10^{-6}

$^{26}\mathrm{Si}(p,\gamma)^{27}\mathrm{P}(\beta^+\nu)^{27}\mathrm{Si}$ reaction branch (shown in Fig. 11) which leads to a rapid reduction of the ^{26}Si equilibrium abundance and a considerable enrichment of the ^{27}P abundance within the period of $t = 0.2 - 20.0$ s. This is shown in Fig. 12. The subsequent $^{27}\mathrm{P}(p,\gamma)^{28}\mathrm{S}$ reaction leads to a higher production of ^{28}S than observed before, but the $^{27}\mathrm{P}(\beta^+\nu)^{27}\mathrm{Si}$ is still the dominant decay mechanism for ^{27}P. At higher mass isotopes only minor changes occur, because of the significantly reduced reaction rate of $^{32}\mathrm{Cl}(p,\gamma)^{33}\mathrm{Ar}$ the β decay of ^{32}Cl dominates the reaction flow, this results in a considerably reduced production of ^{33}Ar.

The results of the network calculations at T_9=0.4 confirm the results of the lower temperature calculations on a faster timescale. Figure 13 shows that the change in the reaction flow at this temperature is characterized by the reaction sequence $^{26}\mathrm{Si}(p,\gamma)^{27}\mathrm{P}(\beta^+\nu)^{27}\mathrm{Si}$ with a weaker side branch $^{26}\mathrm{Si}(p,\gamma)^{27}\mathrm{P}(p,\gamma)^{28}\mathrm{S}$. This is also reflected in the abundances as demonstrated in Fig. 14. It indicates that also at this temperature ^{26}Si and ^{26}Al are considerably reduced while ^{27}P and ^{28}S are enhanced. For higher mass isotopes only minor deviations were caused by the change of reaction rates.

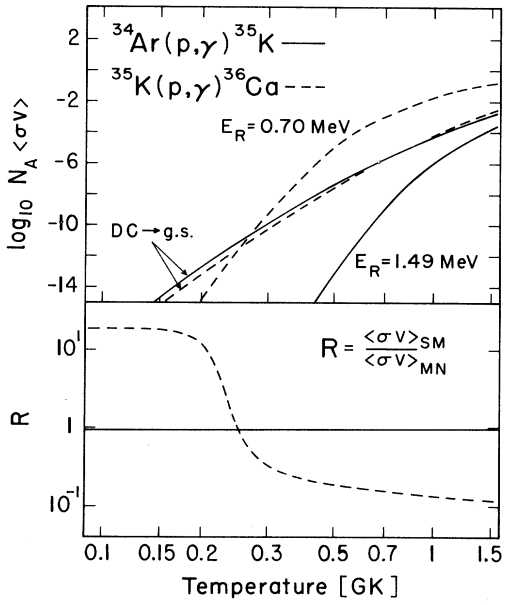

FIG. 7. The figure shows the reaction rate contributions for $^{34}\mathrm{Ar}(p,\gamma)^{35}\mathrm{K}$ (solid lines) and for the subsequent reaction $^{35}\mathrm{K}(p,\gamma)^{36}\mathrm{Ca}$ (dashed lines). The $^{34}\mathrm{Ar}(p,\gamma)$ reaction is dominated by the direct capture to the ground state, the resonance contribution from the first excited level in ^{35}K is negligible. The present rate is in good agreement with the previous estimate as shown in the lower part of the figure. The reaction rate of $^{35}\mathrm{K}(p,\gamma)$ is dominated by a strong resonance at 700 keV. The direct capture to the ground state in ^{36}Ca does however contribute considerably at lower temperatures $T \leq 2.5\times10^8$ K.

V. CONCLUSION

The new reaction rates for proton capture on neutron deficient nuclei in the mass range $A = 23 - 43$ represent

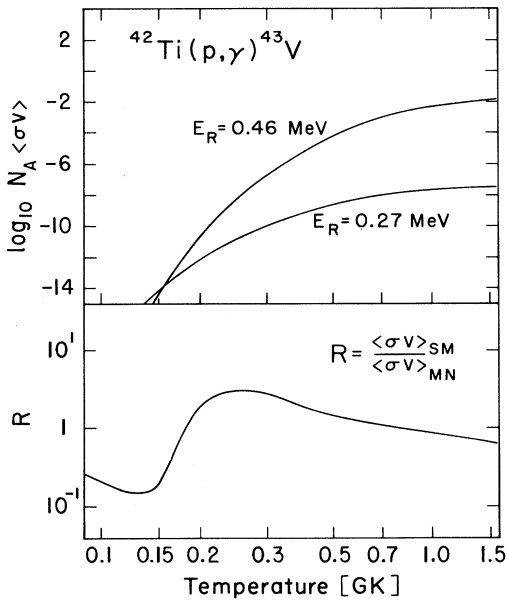

FIG. 8. The reaction rate of $^{42}\mathrm{Ti}(p,\gamma)^{43}\mathrm{V}$ is dominated by the resonance at 460 keV as seen in the upper part of the figure. The lower part shows the ratio between the present reaction rate $\langle\sigma v\rangle_{\mathrm{SM}}$ and the previous estimate $\langle\sigma v\rangle_{\mathrm{MN}}$ from the mirror nucleus ^{43}Ca. The comparison shows that the present rate is in fair agreement with the previous estimate.

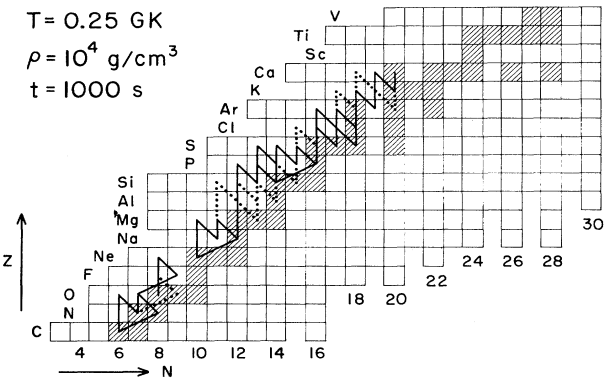

FIG. 9. The figure shows the main reaction flow in the mass range $A = 10$ to $A = 52$ calculated for a constant temperature of $T = 2.5 \times 10^8$ K and a density of 10^4 g/cm^3 over a period of $t = 1000$ s. No changes compared to the reaction path based on previous reaction rate estimates are observed.

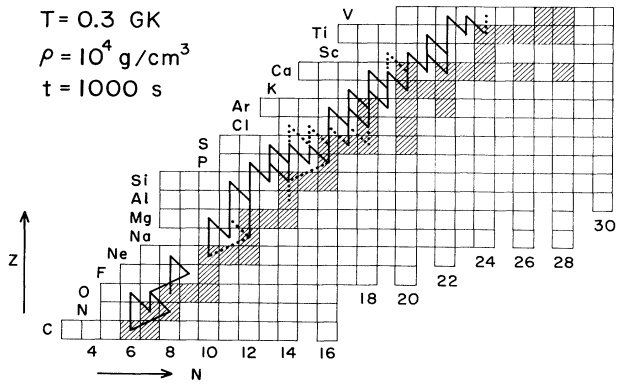

FIG. 11. The figure shows the main reaction flow in the mass range $A = 10$ to $A = 52$ calculated for a constant temperature of $T = 3 \times 10^8$ K and a density of 10^4 g/cm^3 over a period of $t = 1000$ s. Compared to previous calculations [3] the present reaction path passes via $^{26}\mathrm{Si}(p,\gamma)^{27}\mathrm{P}(\beta^+\nu)^{27}\mathrm{Si}$ and an additional branch via $^{30}\mathrm{S}(p,\gamma)^{31}\mathrm{Cl}(\beta^+\nu)^{31}\mathrm{S}$.

a theoretical improvement over the previous estimates which were mainly based on analog structure arguments. The present reaction rates agree in most cases with the previous estimates within 1 order of magnitude. Using the present rates no deviations from the results obtained with the previous rates were observed in the time integrated reaction flux and only minor deviations in the evolution of the isotopic abundances in this mass range.

One major disagreement, however, occurs in the case of $^{26}\mathrm{Si}(p,\gamma)^{27}\mathrm{P}$. The large Thomas-Ehrman shift for the $1/2^+$ ground state in ^{27}P ground state calculated here predicts the $3/2_1^+$ level energy to be much higher than previously anticipated [9]. This enhances the reaction rate by more than 3 orders of magnitude in the temperature range $T = 0.15 \times 10^8 - 1.0 \times 10^9$ K. Also the reaction rate of $^{27}\mathrm{P}(p,\gamma)^{28}\mathrm{S}$ is enhanced over the entire temperature range due to its considerably larger direct capture component. This causes a far

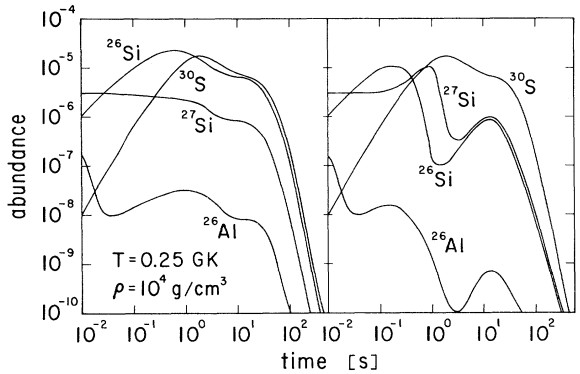

FIG. 10. The figure shows the abundances of ^{26}Al, ^{26}Si, ^{27}Si, and ^{30}S as function of time, calculated for a constant temperature of $T = 2.5 \times 10^8$ K and density of 10^4 g/cm^3. The left-hand side shows the change of the abundances based on the previously estimated rates (MN) and the right-hand side shows the time dependence of the abundances based on the rates presented here (SM). It can be seen clearly that with the present rate ^{26}Si is depleted much faster and converted via ^{27}Si to ^{30}S than in previous calculations.

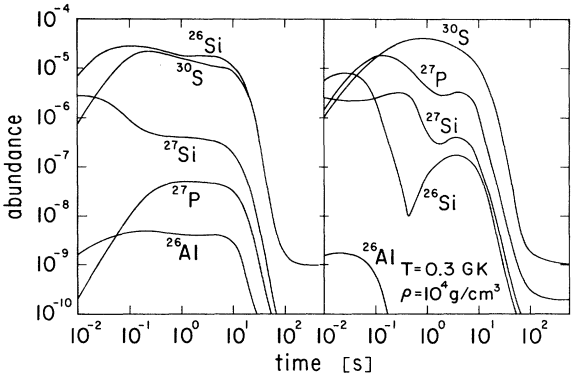

FIG. 12. The figure shows the abundances of ^{26}Al, ^{26}Si, ^{27}Si, ^{27}P, and ^{30}S as function of time, calculated for a constant temperature of $T = 3 \times 10^8$ K and density of 10^4 g/cm^3. The left-hand side shows the change of the abundances based on the previously estimated rates (MN) and the right-hand side shows the time dependence of the abundances based on the rates presented here (SM). Based on the previous rates ^{26}Si remains enriched for more than 20 s. It is, however, clearly to see that with the present rates ^{26}Si depleted rapidly within 0.1 s and converted via ^{27}P to ^{27}Si and ^{30}S, which remains enhanced for approximately 10 s.

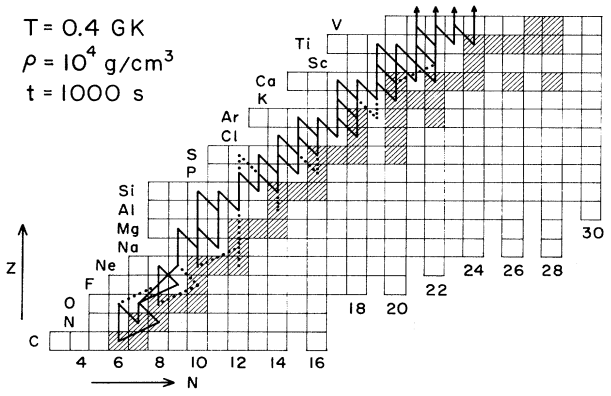

FIG. 13. The figure shows the main reaction flow in the mass range $A = 10$ to $A = 52$ calculated for a constant temperature of $T = 4 \times 10^8$ K and a density of 10^4 g/cm^3 over a period of $t = 1000$ s. Considerable changes compared to the reaction path based on previous reaction rate estimates are observed.

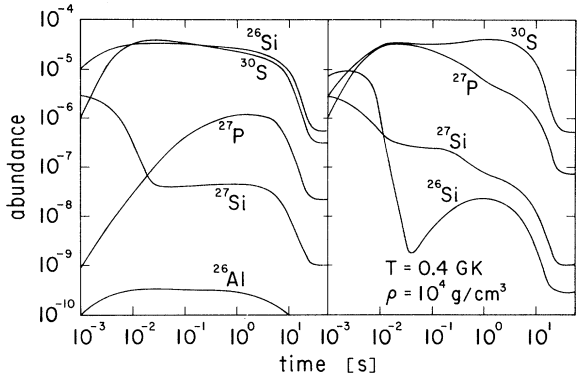

FIG. 14. The figure shows the abundances of ^{26}Al, ^{26}Si, ^{27}Si, ^{27}P, and ^{30}S as function of time, calculated for a constant temperature of $T = 4\times10^8$ K and density of 10^4 g/cm^3. The left-hand side shows the change of the abundances based on the previously estimated rates (MN) and the right-hand side shows the time dependence of the abundances based on the rates presented here (SM). Based on the previous rates ^{26}Si remains enriched for approximately 10 s. Based on the present rates ^{26}Si is depleted rapidly within 0.01 s, converted to ^{27}P and further to ^{30}S.

more rapid destruction of the "waiting point nucleus" ^{26}Si via ^{26}Si$(p,\gamma)^{27}$P$(\beta^+\nu)^{27}$Si and ^{26}Si$(p,\gamma)^{27}$P$(p,\gamma)^{28}$S than previously thought. This has implications for the production of ^{26}Al in hot hydrogen burning. For temperatures $T \geq 2 \times 10^8$ K ^{26}Al is mainly produced by the slow β^+ decay of its enriched progenitor ^{26}Si. For higher temperatures ^{26}Si is now being rapidly depleted reducing therefore the production of ^{26}Al after the freeze-out. As these changes only apply for higher temperatures, $T \geq 2.5 \times 10^8$ K, the possible production of ^{26}Al in novae [27–29] will not be affected.

ACKNOWLEDGMENTS

The authors want to thank F. K. Thielemann, S. Starrfield, S. Shore, and J. Truran for stimulating discussions. This research was supported in part by NSF Grant Nos. PHY88-03035 (University of Notre Dame) and PHY94-03666 (Michigan State University). One of the authors, H. Herndl, acknowledges the support from Project No. RJ0865-PHY by the Fonds zur Förderung der wissenschaftlichen Forschung (FWF), Austria.

[1] R. K. Wallace and S. E. Woosley, Astrophys. J. Supp. **45**, 389 (1981).
[2] A. E. Champagne and M. Wiescher, Annu. Rev. Nucl. Part. Sci. **42**, 39 (1992).
[3] L. Van Wormer, J. Görres, C. Iliadis, M. Wiescher, and F. K. Thielemann, Astrophys. J. **432**, 326 (1994).
[4] C. E. Rolfs and W. S. Rodney, *Cauldrons in the Cosmos* (University of Chicago Press, Chicago, 1988).
[5] P. Decrock, T. Delbar, P. Duhamel, W. Galster, M. Huyse, P. Leleux, I. Licot, E. Lienard, P. Lipnick, M. Loiselet, C. Michotte, G. Ryckewaert, P. Van Duppen, J. Vanhoerenbeeck, and J. Vervier, Phys. Rev. Lett. **67**, 808 (1991).
[6] R. D. Page, G. Vancraeynest, A. C. Shotter, M. Huyse, C. R. Bain, F. Binon, R. Coszach, T. Davinson, P. Decrock, T. Delbar, P. Duhamel, M. Gaelens, W. Galster, P. Leleux, I. Licot, E. Lienard, P. Lipnick, C. Michotte, A. Ninane, P. J. Sellin, C. S. Sükösd, P. Van Duppen, J. Vanhoerenbeek, J. Vervier, M. Wiescher, and P. J. Woods, Phys. Rev. Lett. **73**, 3066 (1994).
[7] S. E. Woosley, W. A. Fowler, J. A. Holmes, and B. A. Zimmerman, At. Data Nucl. Data Tables **22**, 371 (1978).
[8] J. J. Cowan, F.-K. Thielemann, and J. W. Truran, Phys. Rep. **208**, 268 (1991)
[9] M. Wiescher, J. Görres, F.-K. Thielemann, and H. Ritter, Astrophys. Astron. **160**, 56 (1986).
[10] M. Wiescher, J. Görres, B. Sherrill, M. Mohar, J. S. Winfield, and B. A. Brown, Nucl. Phys. **A484**, 90 (1988).
[11] B. A. Brown, A. E. Champagne, H. T. Fortune, and R. Sherr, Phys. Rev. C **48**, 1456 (1993).
[12] A. E. Champagne, B. A. Brown, and R. Sherr, Nucl. Phys. **A556**, 123 (1993).
[13] S. Vouzoukas, C. P. Browne, U. Giesen, J. Görres, S. M. Graff, H. Herndl, C. Iliadis, L. O. Lamm, J. Meissner, J. G. Ross, K. Scheller, L. Van Wormer, M. Wiescher, and A. A. Rollefson, Phys. Rev. **C 50**, 1185 (1994).
[14] W. A. Fowler, G. R. Caughlan, and B. A. Zimmermann, Annu. Rev. Astro. Astrophys. **13**, 69 (1975).
[15] W. A. Fowler, G. R. Caughlan, and B. A. Zimmermann, Annu. Rev. Astro. Astrophys. **5**, 525 (1967).
[16] P. J. Brussaard and P. W. M. Glaudemans, *Shell Model Applications in Nuclear Spectroscopy* (North-Holland, Amsterdam, 1977).
[17] B. A. Brown, A. Etchegoyen, W. D. M. Rae, and

N. S. Godwin, OXBASH, 1984 (unpublished).
[18] B. H. Wildenthal, Prog. Part. Nucl. Phys. **11**, 5 (1984).
[19] B. A. Brown and B. H. Wildenthal, Annu. Rev. Nucl. Part. Sci. **38**, 29 (1988).
[20] W. E. Ormand and B. A. Brown, Nucl. Phys. **A491**, 1 (1989).
[21] E. K. Warburton, J. A. Becker, D. J. Millener, and B. A. Brown, *"The WBMB Shell-Model Interaction and the Structure of* ^{16}O *(2s,1d)*$^{A-16-n}$ *(1f,2p)*^{n} *Levels in A = 31-44 Nuclei with Particular Emphasis on Binding Energies and Energy Spectra,"* BNL Report 40890, 1987.
[22] W. A. Richter, M. G. Van Der Merwe, R. E. Julies, and B. A. Brown, Nucl. Phys. **A523**, 325 (1991).
[23] M. Carchidi, B. H. Wildenthal, and B. A. Brown, Phys. Rev. **C 34**, 2280 (1986).
[24] B. A. Brown and B. H. Wildenthal, Nucl. Phys. **A474**, 290 (1987).
[25] R. G. Thomas, Phys. Rev. **88**, 1109 (1952).
[26] P. M. Endt, Nucl. Phys. **A521**, 1 (1990).
[27] A. Weiss, J. W. Truran, Astrophys. Astron. **238**, 178 (1990).
[28] I. Nofar, G. Shaviv, and S. Starrfield, Astrophys. J. **369**, 440 (1991).
[29] M. Politano, S. Starrfield, J. W. Truran, A. Weiss, and W. M. Sparks, Astrophys. J. (to be published).